# Synthesis of Ligand-Stabilized Metal Oxide Nanocrystals and Epitaxial Core/Shell Nanocrystals *via* a Lower-Temperature Esterification Process

**Daisuke Ito,[†,§,*] Shun Yokoyama,[†] Tatiana Zaikova,[‡] Keiichiro Masuko,[†] and James E. Hutchison[†,‡,*]**

[†]Nanoscience Open Research Initiative, Materials Science Institute and Department of Chemistry and [‡]Department of Chemistry, University of Oregon, Eugene, Oregon 97403, United States, and [§]Nano Science Research Laboratory, US Research Center, Sony Electronics Inc., Eugene, Oregon 97403, United States

**ABSTRACT** The properties of metal oxide nanocrystals can be tuned by incorporating mixtures of matrix metal elements, adding metal ion dopants, or constructing core/shell structures. However, high-temperature conditions required to synthesize these nanocrystals make it difficult to achieve the desired compositions, doping levels, and structural control. We present a lower temperature synthesis of ligand-stabilized metal oxide nanocrystals that produces crystalline, monodisperse nanocrystals at temperatures well below the thermal decomposition point of the precursors. Slow injection (0.2 mL/min) of an oleic acid solution of the metal oleate complex into an oleyl alcohol solvent at 230 °C results in a rapid esterification reaction and the production of metal oxide nanocrystals. The approach produces high yields of crystalline, monodisperse metal oxide nanoparticles containing manganese, iron, cobalt, zinc, and indium within 20 min. Synthesis of tin-doped indium oxide (ITO) can be accomplished with good control of the tin doping levels. Finally, the method makes it possible to perform epitaxial growth of shells onto nanocrystal cores to produce core/shell nanocrystals.

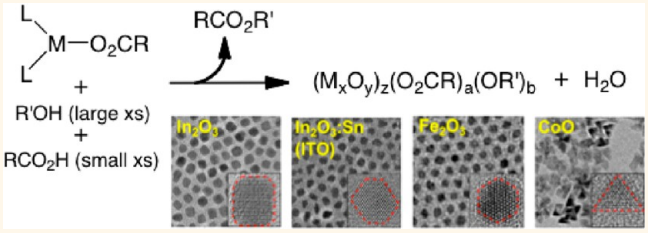


**KEYWORDS:** nanoparticle synthesis · metal oxide nanoparticles · core–shell nanoparticles · doped nanoparticles · geometry control · epitaxial · greener synthesis

Metal oxides, because they are ubiquitous in nature and in technological applications, are among the most widely investigated inorganic substances. The wide range of properties exhibited by these substances has led to their use in practical applications such as pigments, catalysts, fillers, coatings, and electronic materials. The nanoscale forms of these materials, metal oxide nanocrystals, are promising materials for use in catalysts,[1,2] lithium ion batteries,[3,4] solar cells,[5] light emitting diodes,[6] sensors,[7] and transparent electrodes.[8] Their properties can be widely tuned, ranging from semiconductors to metals, through the choice of the framework metal and by introducing impurities (dopants) into the oxides.[1,8,9] In addition, the use of core/shell nanocrystals provides additional opportunities to produce new materials that have remarkably different properties.[10,11]

The range of compositions and the structural diversity possible in this class of nanocrystals will result in a variety of new functional materials, but only if the components of these multimetallic oxide nanocrystals can be precisely assembled. More advanced synthetic methods are needed to tailor the features of the inorganic portion of the nanocrystal (such as size, shape, phase, crystallinity and core composition, including incorporation of substoichiometric metals or dopants) and the specific surface functionality that collectively dictate the material properties.

During the last several decades new synthetic methods have been developed that provide a greater degree of control over these physical attributes. Pioneering methods based upon hydrolysis and sol–gel reactions in aqueous media produced monodispersed colloids,[12] but suffered from a number of limitations.[13] Although the colloids are often monodispersed, particle sizes are large, typically in the hundreds of nanometers. The resulting particles are often amorphous

* Address correspondence to daisukeb.ito@jp.sony.com, hutch@uoregon.edu.

Received for review April 17, 2013 and accepted December 26, 2013.

**Published online December 26, 2013**
**10.1021/nn401888h**

and require heating to induce crystallization. The heating process can alter the initial size and morphology of the particles. Finally, the aqueous reaction environment is complex. As a result, the features of the produced colloids are sensitive to pH, the identity of the anions present, and the methods of mixing in addition to the concentration and temperature. Slight changes in these parameters can have a dramatic influence on the product.[13]

The development of nonaqueous sol–gel chemistry carried out in inert organic solvents eliminates some of the complexity found in aqueous solutions.[14,15] In these approaches, reactive monomers or metal oxide oligomers are produced through elimination reactions, thermal decomposition, or surface-catalyzed reactions.[16] Typical metal–organic precursors include metal acetylacetonates, carboxylates (including acetate and longer chain fatty acids), and halides. They are typically carried out in higher-boiling, inert solvents, for example higher boiling hydrocarbons and long chain or aromatic alcohols, often in the presence of a coordinating solvent, capping agent or surfactant as a stabilizer. These stabilizers include surfactants, long-chain acids or long-chain amines.[17]

Metal carboxylate complexes are useful precursors for metal oxide nanocrystals because they are halide free and are readily available for a wide range of metal ions. The use of long-chain fatty acids, for example oleic acid, as coordinating ligands in the production of nanocrystals avoids the toxicity of many surfactants and can be used to control the morphology of the nanocrystals.[18,19] In a typical metal oxide synthesis, the metal carboxylate precursors are thermally decomposed to produce reactive species.[20] Reactions are often conducted at high temperatures (>300 °C) to facilitate rapid and complete conversion of the precursor.[21–24] To achieve monodisperse nanocrystals, the reaction conditions are chosen to separate the nucleation and growth phases of the reaction using either the "hot injection" or "heat up" method.[25] Regardless of the approach, high temperatures are typically required to solubilize precursors, decompose the precursors, and/or convert (anneal) amorphous nanoparticles to the crystalline form.

These thermal decomposition reactions present some challenges for producing nanocrystalline materials with specific structures and compositions. They are sensitive to variations in temperature and reagent mixing, making it difficult to control and reproduce synthesis conditions.[15] Uniform doping or production of mixed oxide nanocrystals can be difficult because each metal precursor has a different decomposition temperature.[26] The production of core/shell structures is challenging because nucleation of new particles from the shell precursor competes with shell growth onto the core material. Finally, high temperatures preclude the use of thermally sensitive organic chemical functionality within stabilizers and ligands.

Alternatives to thermal decomposition would permit a more precise introduction of framework, dopant, or shell metals, while increasing yields and shortening reaction times needed to produce crystalline nanoparticles. Although most syntheses are conducted at temperatures where thermal decomposition is the primary pathway to produce reactive metal species, a few reports suggest that esterification (or amidation) reactions of the metal carboxylate might provide an approach to produce reactive species at lower temperatures. Recently, alcoholysis[22,27] and aminolysis[28] of metal precursors have been reported as alternative synthetic routes to metal oxide nanoparticles. However, both of these approaches still require reaction temperatures above 290 °C[22,27,28] where thermal decomposition is a competitive reaction pathway.

Because a number of metals catalyze the reaction of carboxylic acids with alcohols to produce organic esters at temperatures below 200 °C,[29,30] we thought that a simple and reliable route for low temperature synthesis of nanocrystals would result if we could accelerate the conversion of metal carboxylates to metal hydroxides through an esterification in *neat* alcohol. Some evidence for the viability of this approach has been reported for the production of cobalt- and nickel-doped zinc oxide nanoparticles by Singhal *et al.*[31]

Here we report a simple, lower temperature (<230 °C) esterification process for synthesizing monodispersed oxide nanocrystals. The method provides a rapid approach to produce monodisperse, crystalline materials in high yield. The synthetic method applies to a wide range of nanocrystals, including indium oxide ($In_2O_3$), tin-doped $In_2O_3$ (ITO), iron oxide ($\gamma$-$Fe_2O_3$), manganese oxide ($Mn_3O_4$), cobalt oxide (CoO), and zinc oxide (ZnO). In all cases, a rapid esterification reaction produces high quality materials in good yields. We demonstrate some advantages of the synthesis by controlling tin doping in ITO and growing epitaxial core/shell nanocrystals ($\gamma$-$Fe_2O_3$/MnO and ZnO/ $\beta$-$Ga_2O_3$).

## RESULTS AND DISCUSSION

**Synthesis of Oleic Acid-Stabilized Indium Oxide Nanocrystals.** We chose indium oxide as an initial target to develop a lower temperature synthesis because of our interest in tin-doped indium oxide[24] and because it was experimentally possible to investigate the fate of the organic components by proton NMR and IR spectroscopies. Our aim was to react the metal carboxylate (initially indium(III) acetate) with a large excess of alcohol that we thought would produce a reactive metal hydroxo species that would subsequently condense[32] to form metal oxide nanocrystals. Caruntu *et al.* have reported synthesis of $In_2O_3$ nanocrystals through the reaction of oleyl alcohol and indium acetate at 320 °C but reported no evidence of ester formation.[33] However, indium acetate is not soluble in oleyl alcohol unless the mixture is heated to over 245 °C.

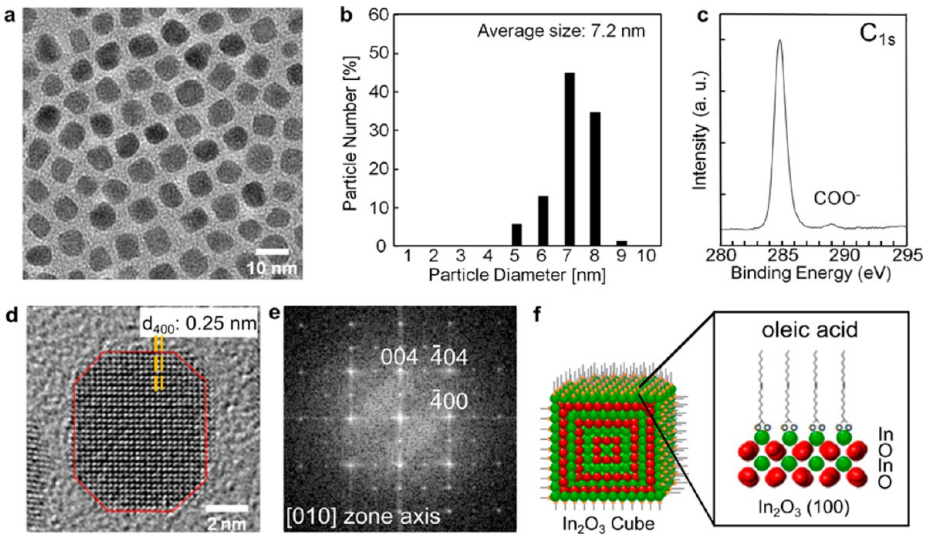


**Figure 1. Low magnification TEM image (a), TEM size analysis (b), XPS $C_{1s}$ spectrum (c), HRTEM image (d), FFT of the high-resolution image (e), and schematic structures (f) of $In_2O_3$ nanocrystals synthesized at 230 °C, respectively.**

To improve the solubility in oleyl alcohol, the acetate ligands were exchanged for oleate ligands that have analogous long-chain structure to the alcohol. Compared to the acetate complex, indium oleate remains soluble in oleyl alcohol even at room temperature. The use of oleic acid and oleyl alcohol has the added benefit that they are derived from nontoxic natural fats and oils, as is the byproduct of the esterification, oleyl oleate.[34] To produce the oleate complexes, metal acetates were heated in oleic acid at 150 °C to replace the acetate ligands with oleate ligands.[35] Solutions of metal oleates were used without further purification. The metal oleate complexes can be synthesized and isolated by other methods;[21,22] however, we found that producing the oleate complex *in situ* worked well.

The reactivity of the indium oleate with oleyl alcohol was investigated. Because the thermal decomposition of indium carboxylates occurs between 270 and 340 °C,[35] we examined temperatures well below 270 °C to avoid thermal decomposition. As a control we confirmed the stability of indium(III) oleate in oleic acid at 250 °C over a 2 h period by proton NMR analysis of aliquots of the solution.

We next tested the traditional "heat up" and "hot injection" approaches to nanocrystal formation. In the heat up approach, the metal oleate solution containing a small excess of oleic acid was heated up with a large excess of oleyl alcohol. In the hot injection trials, the metal oleate solution in oleic acid was injected into oleyl alcohol heated to 230 °C. To our surprise, both approaches failed. Using the heat up method we were not able to control the size of the product nanocrystals. Our previous results heating up indium acetate in oleyl alcohol required a careful control of the temperature to avoid precipitation.[24] During rapid (~2 mL in 5 s) hot injection, the formation of water and precipitation of metal oxide solids were observed during and after the injection period.

We next attempted injecting the solution at rates slow enough that water could be swept away and precipitation did not occur. The addition of a 1:3.3 mixture of indium(III) oleate in oleic acid at 0.2 mL/min into a large excess (33.5 x) of oleyl alcohol, coupled with a flow of nitrogen to flush water vapor from the headspace over the reaction mixture, led to reproducible nanocrystal formation without precipitation. The nitrogen flow prevented condensation of water droplets during the reaction. Upon addition of the indium oleate solution, the color of the solution turns from pale yellow to light blue, and finally to yellow, suggesting the formation of nanoparticles during the course of the addition. The presence of nanoparticles was confirmed at 60 s into the addition by TEM analysis of an aliquot of the reaction mixture that was removed and quenched by cooling. The nanocrystals were precipitated and washed to remove any free acid, alcohol, and ester prior to characterization.

Because impurities in solvents and capping agents are known to influence nanocrystal formation,[36] we compared the $In_2O_3$ nanocrystals produced using reagent grade oleic acid, technical grade oleic acid, and even olive oil, by TEM and found that the same sized nanocrystals were produced in each case. For subsequent syntheses the technical grade reagents were used due to their significantly lower cost.

Figure 1a shows transmission electron microscope (TEM) images of $In_2O_3$ nanocrystals. The average diameter of the nanocrystals is 7.2 nm (±0.7 nm) (Figure 1b). Powder X-ray diffraction (XRD) (Supporting Information) confirms that the structure of the nanocrystal core is $In_2O_3$. Figure 1c shows an X-ray photoelectron spectrum (XPS) of the $C_{1s}$ core levels for this sample. The peak at 289.0 eV is assigned to the carboxylate carbon,[37,38]

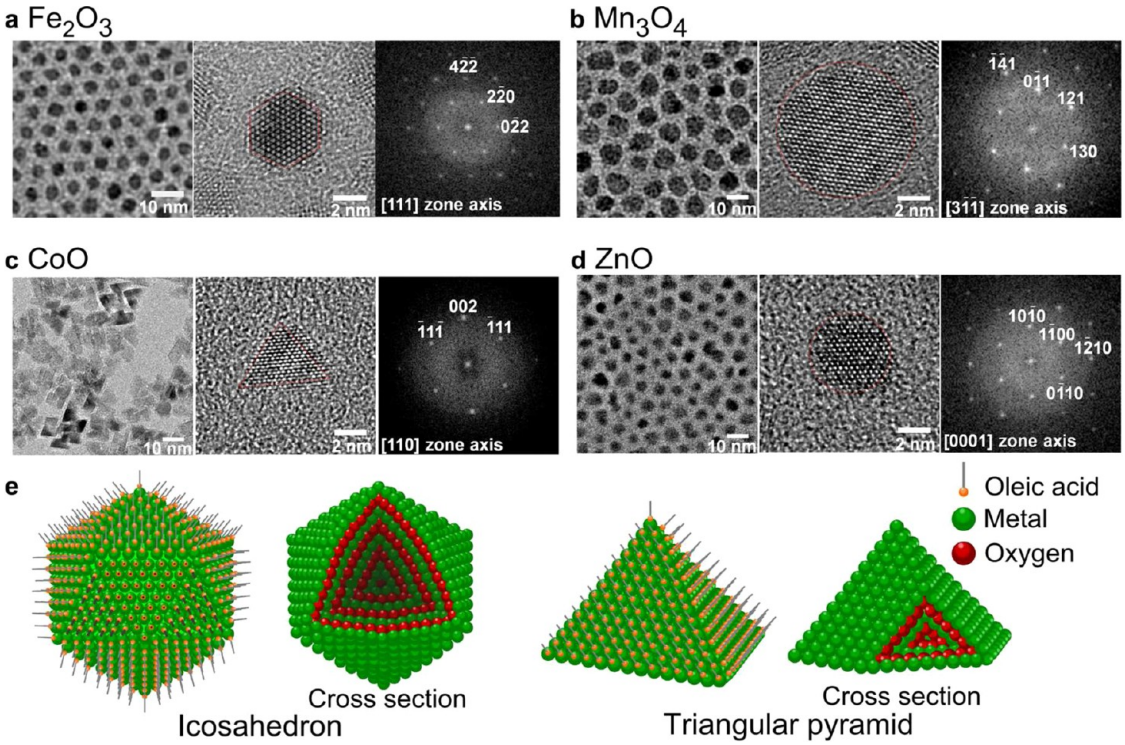


**Figure 2. Low and high magnification TEM images and FFT images of $\gamma$-$Fe_2O_3$ (a), $Mn_3O_4$ (b), CoO (c), and ZnO (d) nanocrystals synthesized at 230 °C, respectively. Schematics of a layered icosahedron and a layered triangular pyramid (e) are shown to support the discussion of the faces displayed for these possible structures (see the main text).**

suggesting that the surface is passivated by oleic acid. The ligand shell composition was further investigated by time-of-flight secondary ion mass spectroscopy (ToF-SIMS) (Supporting Information) that confirmed that the ligand shell is primarily oleic acid, containing less than 2% oleyl alcohol. The interparticle edge-to-edge distance in TEM is 2.5−3.0 nm. This value is shorter than expected for two layers of extended oleic acid (4.0 nm) and implies some degree of interdigitation of the alkyl chains of ligands coordinated to neighboring nanocrystals.[39,40]

Figure 1 panels d and e show a HRTEM image of a typical $In_2O_3$ nanocrystal and its fast Fourier transform (FFT), respectively. The shape of these $In_2O_3$ nanocrystals is a truncated cube and the surface is surrounded mostly by {001} facets. This is surprising for $In_2O_3$ because typically the {001} facets are unstable because of their strong polarity[41] and therefore, {111} facets dominate as the most stable planes. The importance of the surface energies in the growth of the $In_2O_3$ nanocrystals has been discussed and, in general, the trend is $\gamma(111) < \gamma(011) < \gamma(211) < \gamma(001)$.[41] However, if the $In_2O_3$ nanocrystals were formed *via* hydroxide species, there are several reports that {001} facets are stable and form cubes.[42,43] Agoston *et al.* reported that the {001} planes become more stable than {111} planes ($\gamma(001) < \gamma(111)$) when the surface is terminated by water or hydroxide.[41] The presence of surface hydroxy species is suggested by the peak at 531.7 eV in the $O_{1s}$ XPS spectrum[44] (Supporting Information). The {001} facets of $In_2O_3$ nanocrystals are polar, layered structures of metal−oxygen−metal coordination terminated by oleic acid (Figure 1f).

**Synthesis of Ligand-Stabilized Metal Oxide Nanocrystals from Iron, Manganese, Cobalt and Zinc Precursors.** Our success in producing low dispersity, crystalline, oleic acid-stabilized $In_2O_3$ nanocrystals in high yield led us next to explore the generality of the synthesis. We evaluated the efficacy of the same synthesis conditions developed for indium for a series of other metals. In most cases, high yields of the nanocrystals were achieved. The reaction did not produce nanocrystals in the case of antimony, copper, and silver. In the case of zinc oxide, the poorer solubility of the precursor resulted in lower yield. The characterization of each of the nanocrystal products is described below.

Figure 2 show TEM images of $\gamma$-$Fe_2O_3$, $Mn_3O_4$, CoO, and ZnO nanocrystals. All the nanocrystals are single-crystalline and nearly monodisperse even though they were all produced at significantly lower temperatures than previous approaches. The crystal structures of each were determined by HR-TEM and confirmed by powder XRD. The $\gamma$-$Fe_2O_3$ nanocrystals average 4.0 nm (±0.3 nm) in diameter and are icosahedrons or octahedrons surrounded by {111} facets (Figure 2a). The $Mn_3O_4$ (Marokite) nanocrystals are 9.2 nm (±1.1 nm) in diameter and spherical (Figure 2b). The CoO nanocrystals are triangular (6.6 nm (±1.6 nm) on each side) with {111} facets (Figure 2c). Figure 2d shows that ZnO nanocrystals exhibit both spherical and triangular shapes.

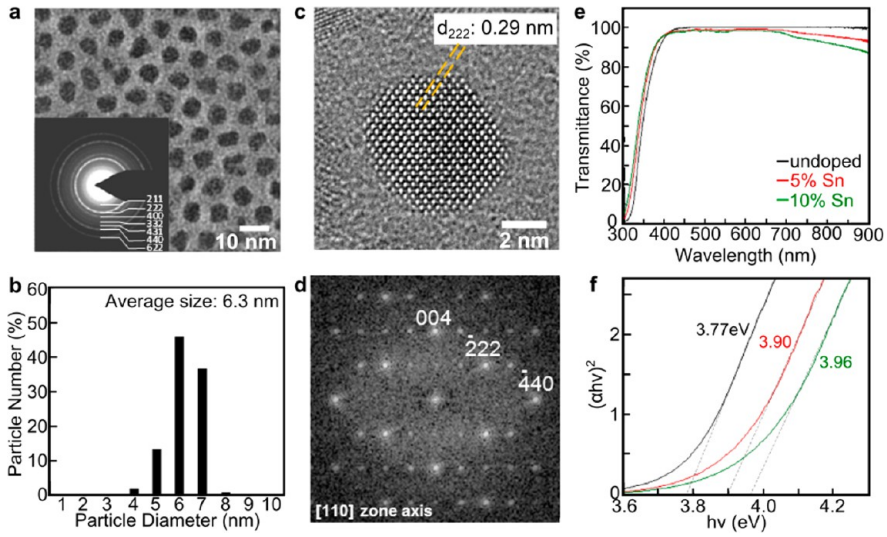


**Figure 3. A low magnification TEM image (a), size analysis (b), a HRTEM image (c), a FFT image (d) of 10% tin-doped ITO nanocrystals, respectively. UV−vis spectra (e), replot of UV−vis spectra (f) of ITO nanocrystals with various tin concentrations, respectively. Solutions of nanocrystals were prepared at 33 $\mu$g/mL in toluene for optical analysis.**

The average diameter of the spherical ZnO nanocrystals is 5.6 nm (±1.0 nm). Preliminary results suggest that the sizes of the nanocrystals produced depend upon the reaction conditions, most notably the reaction temperature and concentration of oleic acid. The dependence of core size on these reaction parameters is currently under investigation.

The range of nanocrystal shapes of those metal oxides is remarkable. Spherical particles likely dominate when surface defects are needed to minimize surface energies of the nanocrystal. On the other hand, faceted particles will have different mechanisms to minimize surface energies. For example, both $\gamma$-$Fe_2O_3$ and CoO nanocrystals have {111} facet planes that are polar planes analogous to those described for the $In_2O_3$ nanocrystals above. If $\gamma$-$Fe_2O_3$ (space group: $P4_132$) and CoO (space group: $Fm\bar{3}m$) are surrounded by {111} planes, the shape can be predicted as an icosahedron, a triangular pyramid, or an octahedron (Figure 2e). The different shapes observed for these nanocrystals are consistent with those previously reported in the literature[45,46] and likely result from interactions between the oleic acid stabilizer and the stable polar crystal planes for each shape. It appears that oleic acid helps define crystal shapes as well as acts as a reagent in the esterification.

The surface chemistries of each of these nanocrystals were investigated by XPS and ToF-SIMS (these data are provided in the Supporting Information). In the XPS spectra, the spectra for the metal ions are consistent with the oxide forms identified by XRD. The $O_{1s}$ spectra display peaks for the metal oxide and in all cases a smaller component at higher binding energy (531.1−537.7 eV depending upon the metal) consistent with a metal hydroxide species.[47] Combined, the XRD results and the relatively smaller $O_{1s}$ peak due to hydroxide suggest that there are hydroxy groups on the surface of the nanocrystals. As in the case of the $In_2O_3$ nanocrystals, the main surface ligand detected by ToF-SIMS is oleic acid. In each case, small amounts of oleyl alcohol (7−11%) are present in the ligand shells for these nanocrystals.

**Doped Nanoparticles: Tin-Doped $In_2O_3$.** We synthesized tin-doped indium oxide (ITO) nanocrystals to explore whether it is possible to control precisely the doping levels needed for practical applications. ITO nanocrystal dispersions are deep blue, which is clearly different from the yellowish color of the nondoped $In_2O_3$ nanocrystal dispersion (see Supporting Information Figure S2). Figure 3a and the inset show a TEM image of 10% tin-doped ITO nanocrystals and a selected area electron diffraction (SAED) pattern, respectively. These data show that the ITO nanocrystals are monodisperse and the matrix phase of the nanocrystals is cubic $In_2O_3$ without any other phases. Their average diameter is 6.3 nm ± 0.6 nm (Figure 3b). Figure 3 panels c and d show a HRTEM image of a typical ITO nanocrystal and its FFT, respectively. The shape of the ITO nanocrystal is not a cube, but a truncated octahedron that is surrounded by {001} and {111} facets. The {111} planes of $In_2O_3$ are also partially polar planes that may be passivated by oleic acid.

Figure 3e shows the dependence of the UV−vis transmission spectra upon the tin concentration for the ITO nanocrystal dispersions. All of dispersions have over 98% transmittance in the visible range and show reflections in the infrared range that are explained by free-electron vibrations.[48] The blue shift of the bandgap resulting from increasing tin concentration can be explained by the Burstein−Moss effect.[48] In Figure 3f, the UV−vis transmittance spectra (Figure 3e) are replotted as absorption versus energy so that the optical

**TABLE 1. Summary of Compositions, Yields, Burstein–Moss Shift, and Estimated Free-Electron Concentrations of ITO Nanocrystals**

| | In (%) | Sn (%) | % yield | Burstein–Moss shift[a] (eV) | estimated free-electron concentration[a] ($cm^{-3}$) |
|---|---|---|---|---|---|
| $In_2O_3$ | 100 | 0.0 | 92 | 0.0 | 0.0 |
| 5% ITO | 95.3 | 4.7 | 92 | 0.13 | $2.2 \times 10^{19}$ |
| 10% ITO | 89.5 | 10.5 | 94 | 0.19 | $3.9 \times 10^{19}$ |

[a] Normalized to pure $In_2O_3$ nanocrystals.

band edges can be estimated and the Burstein–Moss shifts can be determined. Compared to that of nondoped $In_2O_3$ nanocrystals, Burstein–Moss shifts of 0.13 eV (5% Sn) and 0.19 eV (10% Sn) were observed, corresponding to $2.2 \times 10^{19}$ $cm^{-3}$ and $3.9 \times 10^{19}$ $cm^{-3}$ of free-electron concentrations. The free-electron concentration nearly doubles with the doubling of the tin concentration. Although the size of nanocrystals ($d \sim 6$ nm) is in the range of quantum confinement[49] or full depletion of carrier electrons,[50] the ITO nanocrystals show significantly high values of free-electron conscentrations suggesting a transparent metallic nanomaterial.

Table 1 shows summarized values of the ITO nanocrystals. Elemental compositions were determined from the ratios of the XPS peaks of $In_{3d}$ and $Sn_{3d}$. The composition gap between initial precursors and nanocrystals is accurate within ± 0.5 atomic % by several repeated measurements. These results suggest that the rapid esterification leads to simultaneous and complete decomposition of the precursors. The yield of nanocrystals at 230 °C is greater than 90% yield by measuring the weight of products in a gram-scale synthesis. The catalytic esterification enables high yield synthesis of ITO nanocrystals as well as accurate doping for designing optical absorption, free-electron concentration, and work functions.

**Epitaxial Core/Shell Nanocrystals: $\gamma$-$Fe_2O_3$/MnO and ZnO/$\beta$-$Ga_2O_3$.** Inorganic core/shell nanocrystals[10,11,51] have become important functional materials because crystalline shells can expand the range of interesting new physical and chemical properties as a class of hybrid nanomaterials; however, their synthesis requires greater control of the growth chemistry. Compared with amorphous shells (e.g., $SiO_2$ or $Al_2O_3$), the production of crystalline shells requires nanocrystal cores for their seed-mediated epitaxial growth in order to prevent undesirable nucleation, dumbbell formation,[52] and aggregation. We evaluated our new synthetic approach for its efficacy for core/shell formation using two epitaxial examples: $\gamma$-$Fe_2O_3$/MnO and ZnO/$\beta$-$Ga_2O_3$ core/shell nanocrystals. $\gamma$-$Fe_2O_3$/MnO nanocrystals possess novel magnetic properties as a result of their core/shell structure.[52–54] ZnO/$\beta$-$Ga_2O_3$ nanocrystals are interesting because of their optical properties. In this case, the application of a wide band gap ($E_g$: 4.6 eV, $Ga_2O_3$) semiconducting shell onto a narrow band gap ($E_g$: 3.4 eV, ZnO) core should result in a higher band-edge luminescence than single component semiconductor nanocrystals (e.g., CdSe/ZnS core/shell quantum dots)[55,56] because the surface defects of the crystal core are passivated by the wide bandgap material. In addition, a $\beta$-$Ga_2O_3$ shell is chemically inert and would prevent dissolution of ZnO under acidic conditions. The dissolution of ZnO not only degrades the nanomaterial, but is also the origin of toxicity for ZnO nanomaterials.[57,58]

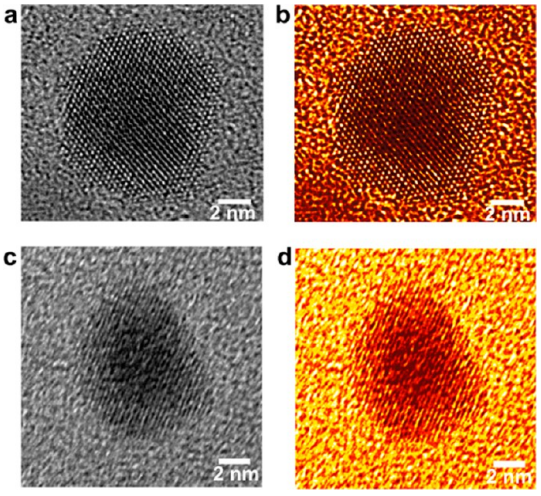


**Figure 4. A HRTEM image (a) and the FFT filtered image (b) of a typical core/shell nanocrystal of $\gamma$-$Fe_2O_3$ (core)/MnO (shell). A HRTEM image (c) and the FFT filtered image (d) of a typical core/shell nanocrystal of ZnO (core)/$\beta$-$Ga_2O_3$ (shell).**

Our esterification approach produces both $\gamma$-$Fe_2O_3$/MnO and ZnO/$\beta$-$Ga_2O_3$ core/shell nanocrystals. First, the cores are synthesized and purified as described earlier. The purified cores were then dissolved in oleyl alcohol and heated to 160 °C under flowing nitrogen. Next, the metal oleates needed to form the shell were injected into the solution along with excess oleic acid, and the reaction was maintained at this temperature for 1 h. To prevent nucleation of new nanoparticles from the shell precursor, the temperature of solution must be kept lower than nucleation temperatures for that metal oxide and oxygen must be excluded.

Figure 4 panels a and b show a HRTEM image and the FFT filtered image of a typical core/shell nanocrystal of $\gamma$-$Fe_2O_3$/MnO. A 2 nm-thick MnO shell was grown epitaxially onto the $\gamma$-$Fe_2O_3$ core. The size of the core is approximately 4.5 nm, corresponding to the diameter of the seeds used in this synthesis. The HRTEM image

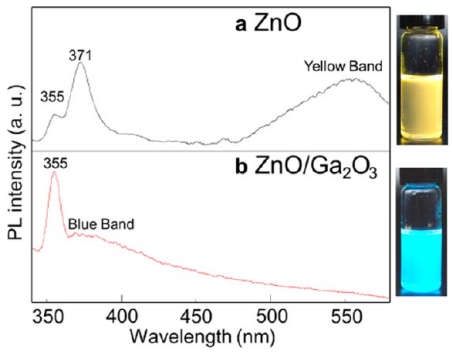


**Figure 5. Photoluminescence spectra of ZnO nancrystals (a) and ZnO/$\beta$-$Ga_2O_3$ core/shell nanocrystals (b) excited at 320 nm by a filtered Hg UV source.**

shows a *d*-spacing of 0.30 nm, indicating $\{110\}^1$ planes of MnO which have an epitaxial relationship with the $\{220\}$ planes of $\gamma$-$Fe_2O_3$ (the lattice mismatch between the structures is 5.6%).

Figure 4 panels c and d show a HRTEM image and the FFT filtered image of a typical core/shell nanocrystal of ZnO/$\beta$-$Ga_2O_3$. A 2 nm-thick crystalline $Ga_2O_3$ shell was grown onto a ZnO core. Adjacent lattice fringes with a *d*-spacing of 0.28 nm were obtained, which correspond to the (002) lattice planes of $\beta$-$Ga_2O_3$. Because the lattice mismatch between the (10−10) planes of ZnO (Figure 4d) and (002) lattice planes of $\beta$-$Ga_2O_3$ is very small (0.1%), a $\beta$-$Ga_2O_3$ shell layer was grown epitaxially on the ZnO nanocrystal.

Figure 5 shows photoluminescence spectra of *n*-hexane dispersions of ZnO nanocrystals and ZnO/$\beta$-$Ga_2O_3$ core/shell nanocrystals excited at 320 nm. In Figure 5a, the emission peaks at 355 nm (3.49 eV), 371 nm (3.34 eV), and a yellow emission band centered at 560 nm (2.21 eV) are assigned to free exciton recombination, bound exciton recombination with ionized defects, and ionized oxygen vacancies in ZnO, respectively.[59,60] The ZnO/$\beta$-$Ga_2O_3$ nanocrystals show a very different emission spectrum. The dominant emission peak is now at 355 nm (compared with 371 nm in ZnO) and the yellow emission band disappears. These results suggest that surface oxygen defects present in ZnO are passivated by the addition of the $Ga_2O_3$.[59,60] The bright blue emission band centered at 370 nm (3.35 eV) in the spectrum of the core/shell structure is due to oxygen vacancies in the $\beta$-$Ga_2O_3$ shell.[61,62]

**Mechanistic Insights into the Formation of Oleic Acid-Stabilized Metal Oxide Nanocrystals.** On the basis of the products formed, our observations made during synthesis, control experiments, and spectroscopic studies performed on the indium system we were able to gain some insights regarding nanocrystal formation under the lower temperature conditions studied here. In each case, a crystalline metal oxide core is formed during synthesis without any need for extended annealing that is typically needed for nanocrystals produced by thermal decomposition. Surface analysis shows that some metal hydroxy species are present on the surface and that the predominant stabilizer is oleic acid.

Additional observations shed some light on the role of the alcohol, metal complexes, water, and excess oleic acid. When indium oleate was heated in oleic acid without added oleyl alcohol at 230 °C for 1 h the solution remained colorless and the proton NMR of the complex remained unchanged. When the complex is added to oleyl alcohol, fine bubbles of water are observed, resulting in the formation of foam across the surface of the reaction mixture. If water is allowed to condense in the reaction vessel and drops back into the heated solution, the drops boil violently and a precipitate is formed. The same result is obtained if water is deliberately added. Color changes suggest that nanoparticles are forming (confirmed by TEM measurements) within 60 s of the beginning of the metal oleate addition. During the time frame for these reactions, the production of water and formation of the ester does not occur without added metal, suggesting that the metal ion and/or its reaction products act as catalysts for esterification. Finally, the additional oleic acid used during the reaction functions effectively to control the nucleation of the $In_2O_3$ clusters during the rapid catalytic esterification. If no excess oleic acid is used, larger aggregates are formed.

These observations were augmented by IR and $^1$H NMR studies of the indium reaction mixtures and several control solutions. Figure 6a shows NMR spectra of the methylene protons next to the carboxylic acid and ester functionality for mixed solutions of oleyl alcohol and oleic acid after heating at 230 °C for 5 min with, and without, indium oleate (the whole spectral range of the NMRs are available in Supporting Information Figure S1). From the increase in the two triplet signals associated with the ester and disappearance of the triplet signal due to the acid, it is clear that esterification between oleic acid and oleyl alcohol proceeds within five minutes, but only in the presence of indium oleate.

Figure 6b shows FT-IR spectra of the solution after the esterification. A sharp peak at 1710 $cm^{-1}$, broad bands ranging from 1520 to 1630 $cm^{-1}$ and from 1720 to 1740 $cm^{-1}$ are assigned to C═O symmetric stretch from oleic acid, asymmetric COO stretch from metal carboxylates, and ester carbonyl stretch, respectively.[27,28] At 230 °C, the peaks for both oleic acid and indium oleate disappear, suggesting that the esterification is complete within five minutes, consistent with the NMR results. Figure 6c shows the time dependence of the esterification and decomposition of indium oleate at 230 °C based upon the FT-IR peaks of the acid, metal carboxylate, and ester. During the first 50 s of esterification, oleic acid is consumed very rapidly, but the indium oleate remains constant. Once most of the acid is depleted, the indium oleate is consumed rapidly with the continued production of

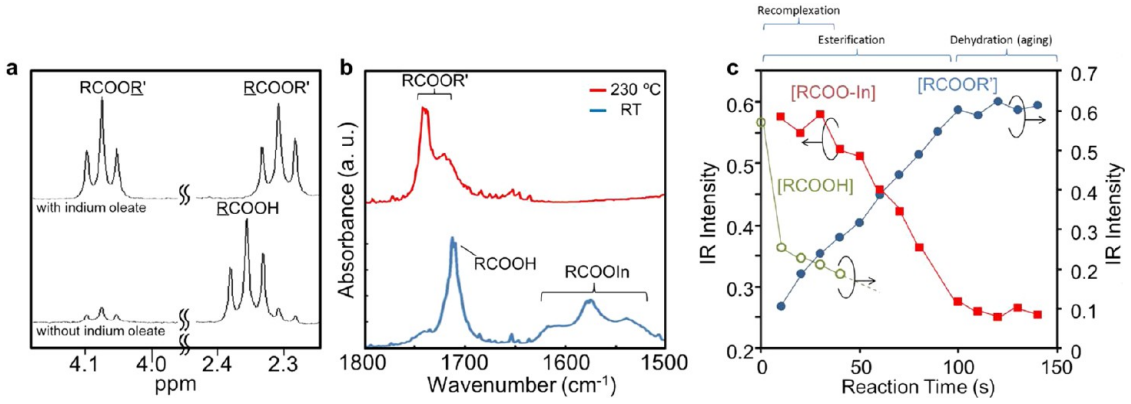


**Figure 6. NMR spectra of mixed solutions of oleyl alcohol and oleic acid after heating at 230 °C for 5 min with and without indium oleate (a). FT-IR spectra of the mixed solutions of oleyl alcohol and oleic acid after heating at 230 °C for 5 min with indium oleate (b). Conversion of oleate complexed indium (RCOOIn) to oleyl oleate (RCOOR′) versus time in the reaction at 230 °C (c). Oleic acid (3.3 mmol) and indium oleate (1 mmol) were dissolved in 12.5 mL (33.5 mmol) for these experiments. The IR intensities in panel c are normalized to the common peak at 1465 $cm^{-1}$.**

ester and nucleation of $In_2O_3$ (determined by TEM). The other metal oleates display similar reactivities.

Given the thermal stability of indium oleate at 230 °C, but its rapid reaction to produce ester in the presence of oleyl alcohol, the initial step of the synthesis is the reaction of the alcohol with the metal carboxylate to form the ester and a metal hydroxy species eq 1. Although IR studies suggest that the ester formation continues, the amount of signal due to the complexed oleate does not decrease until all of the free oleic acid is consumed. Given that esterification at this temperature does not occur without the metal, the continued production of ester suggests that the free acid is being consumed by a metal-catalyzed esterification reaction eq 2. Later in the addition, it is also possible that the growing nanocrystals can catalyze this reaction as well. Once the concentration of the indium hydroxy species increases it can condense with other hydroxy species in a condensation reaction to nucleate and grow nanocrystals eq 3. Nanocrystal formation by condensation of the metal hydroxide species is supported by other examples in the literature[32] and studies of the thermal decomposition of hydroxy indium(III) diacetate.[63] In the latter case, decomposition begins at 207 °C producing water and acetic acid. This finding is also consistent with our observation that at lower temperatures (180−200 °C) the acid is consumed by esterification, but there is no condensation to produce nanoparticles. The presence of some surface hydroxy groups observed in the XPS is consistent with a growth mechanism involving a M−OH species.

$$L_2In(O_2CR) + R'OH \rightarrow L_2InOH + RCO_2R' \quad (1)$$

$$RCO_2H + R'OH \xrightarrow{L_2InOH} RCO_2R' + H_2O \quad (2)$$

$$2L_2InOH \rightarrow L_2In{-}O{-}InL_2 + H_2O \quad (3)$$

We expect that the water generated in eqs 2 and 3 might accelerate the hydrolysis of metal carboxylates

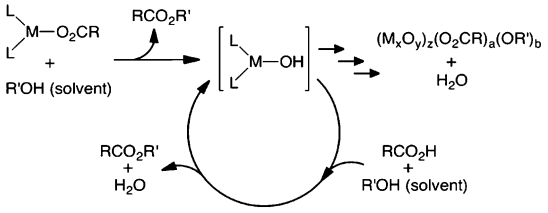


**Scheme 1. Nanocrystal Formation from Metal Oleates at Lower Temperature in Neat Oleyl Alcohol with Excess Oleic Acid**

to metal hydroxides that are subsequently dehydrated to metal oxides eq 3. However, the best control over nanocrystal formation occurs when water is generated relatively slowly and swept away by the nitrogen flow. On the basis of these observations, controls, and spectroscopic studies, and the similar reactivity observed for the other metal oxides studied, we propose that these three steps make up the overall nanocrystal formation reaction shown in Scheme 1.

Within Scheme 1, L designates the various ligands that are bound to the metal throughout the reaction lifetime, including acid, hydroxy, other metal oxide fragments and alcohol. The initial reaction between the metal oleate and the solvent generates the ester and the metal hydroxy species. The hydroxy species can dehydrate to form M−O−M bonds, but in the early stages of reaction when the concentration of oleic acid is higher, a metal catalyzed esterification (the lower loop in the scheme) competes with dehydration. The fact that the IR signals due to the metal oleate do not decrease until after the free acid is consumed is consistent with this reaction pathway. As the free acid is consumed, the dehydration reaction, that is facile about 207 °C, competes and leads to nanocrystal formation.

## CONCLUSIONS

We have developed a lower-temperature esterification reaction pathway for the synthesis of monodispersed $In_2O_3$, ITO, $\gamma$-$Fe_2O_3$, $Mn_3O_4$, CoO, and ZnO

nanocrystals using green and benign oleyl alcohol as a solvent and oleic acid as a ligand and control reagent. The approach is rapid, easily controlled, and results in generally high yields. The lower temperature and enhanced control of the chemical reactivity permits synthesis of precisely doped nanocrystals and core/shell nanocrystals that enhance the functionalities of these nanocrystals. In the case of the doped nanocrystals, the esterification reaction addresses a significant challenge in the production of these types of nanocrystals from multiple precursors, that is to balance the reactivity of the two precursors.[26] In the case of the core/shell structures, the ability to generate reactive precursors that can contribute to shell growth without resulting in nucleation of new nanocrystals is an advantage. Such lower temperature approaches may also aid in preserving kinetic structures formed in shape-controlled reactions that might be altered if reactions are conducted at higher temperatures.

The lower-temperature approach is possible because the production of a reactive metal hydroxy species results from a rapid chemical reaction, esterification, rather than the more common thermal decomposition pathways. The use of slow injection of a precursor at a constant temperature differs from the traditional hot injection or heat up methods but permits tight control over reaction temperature and precursor addition rate.

Although the scope of core size control has not been fully explored in these studies, the detection of metal hydroxy species on the surfaces of the nanocrystals and the successful synthesis of core−shell species suggest that seeded growth may be one approach to extend the size ranges accessible using this approach.

## METHODS

**Materials.** All of chemicals were purchased from Sigma-Aldrich and used as received. As metal precursors, indium(III) acetate (99.99%), iron(II) acetate (99.99%), cobalt(II) acetate (99.995%), tin(IV) acetate (>99%), zinc(II) acetate (99.99%), manganese(II) acetate (98%), gallium acetylacetonate (99.99%), were used. Oleic acid (90% technical grade or 99% analytical standard) was used for producing metal oleates; oleyl alcohol (85% technical grade) was used as solvent.

**Characterization of Metal Oleate Complexes and Metal Oxide Nanocrystals.** Proton NMR spectra were collected on a Varian INOVA 300 MHz spectrometer and on Bruker Avance III HD 600 NMR spectrometer with Prodigy multinuclear broadband BBO CryoProbe (5 mm sample diameter) at 25 °C in $CDCl_3$ (reference to $\delta$7.26) solution. TEM observation was carried out with a FEI Titan operated at 300 kV. Measurements of size distribution of nanocrystals are expressed as a function of the standard deviations. X-ray photoelectron spectroscopy (XPS) was carried out with a Thermo Scientific ESCALAB 250 X-ray photoelectron spectrometer using a monochromatic aluminum K$\alpha$ X-ray source at 20 kV. Nanocrystal samples were drop-cast from toluene onto clean silicon substrates. The binding energy scale of all measurements was calibrated using the $C_{1s}$ peak at 284.6 eV. TEM samples were prepared by drop-casting or aerosol deposition onto holey carbon grids purchased from Ted Pella. Scanning electron microscopy (SEM) was carried out using a ZEISS Ultra-55. UV−visible (UV−vis) transmittance spectroscopy was performed on an Ocean Optics Jaz spectrometer module with DH-2000-BAL UV-NIR deuterium tungsten halogen light source using 1 cm quartz cuvettes. Photoluminescence spectra were collected on a Hitachi F-4500 fluorescence spectrophotometer at room temperature. XRD patterns were recorded on a Phillips X'Pert Panalytical diffractometer with Cu K$\alpha$ ($\lambda$ = 0.1541 nm) operating at 50 kV and 30 mA with step size 0.05° with 1 s time per step. The solid indium oxide sample was fixed to a zero background quartz substrate with hivac grease. All other oxides were dissolved in toluene and drop cast onto a zero background quartz substrate and allowed to dry before measurement. The ToF-SIMS spectra were acquired on a ToF-SIMS IV instrument manufactured by ION-TOF GmbH, Muenster, Germany. The primary ion beam comprised $Bi_3^+$ ions (25 kV 0.3 pA @ 10 kHz). Spectra were acquired over an area of 100 $\mu$m × 100 $\mu$m. The primary ion dose during the acquisitions did not exceed the static limit (defined here as $2 \times 10^{12}$ ions/cm$^2$). Two drops of 5 mg/mL toluene dispersions were deposited on freshly cleaved mica and dried before measurements.

**General Preparation of Metal Oxide Nanocrystals.** The appropriate metal acetate (1 mmol) was mixed with oleic acid (2 mL) in a 15 mL glass vial and heated to 150 °C for 30 min (or 1 h in the case of indium acetate) under a slow flow of nitrogen to generate the metal oleate complexes. The acetic acid boils off during the reaction. Conversion to the oleate complex was confirmed by proton NMR. Oleyl alcohol (12.5 mL, 33.5 mmol based upon 85% in the technical grade material) was heated to 230 °C in a 50 mL three-necked flask fitted with three septa. Dry nitrogen was introduced through one septum *via* a 20 gauge stainless needle, and the gas flow rate was held at 1−5 sccm. The temperature of the oleyl alcohol was maintained using a heating mantle supplied by a temperature controller connected to a stainless thermocouple inserted through the center septum into the liquid. The third neck of the flask is fitted with a septum containing a larger bore needle or two 20 gauge needles to allow escape of water vapor from the flask without condensation (the reaction setup is shown in the Supporting Information). If water condenses within the flask and drips into the reaction mixture, rapid hydrolysis of the metal precursor leads to immediate precipitation of agglomerated solid. The liquid was stirred magnetically at a rate sufficient to create a vortex down to the stirbar. The hot metal oleate/oleic acid solution was injected through the center septum from a 10 mL polypropylene syringe with a stainless 20 gauge needle with a syringe pump at 0.2 mL/min. During addition of the metal oleate precursor, the color of the reaction mixture changed from clear to colored. A continuous stream of water bubbles occurs throughout the transformation. The flow of nitrogen into the flask sweeps the water out of the headspace above the reaction mixture. After the addition is complete, the solution was kept for 20 min at 230 °C with vigorous stirring. The reaction mixture was then cooled to room temperature, and a mixture of 25 mL of ethanol and 5 mL of methanol was added to precipitate the nanoparticles. The precipitate was isolated by centrifugation for 30 min at 7500 rpm. The solid product was washed six times with ethanol and then dispersed in toluene. The resulting toluene dispersion was centrifuged for five min at 5500 rpm to remove any insoluble solids (if any). There should be no insoluble material after this centrifugation step. The percent yield of each nanocrystal core is calculated from the mass of inorganic core material obtained (determined from the mass obtained and the percent inorganic material remaining after heating to 500 °C in the TGA) and the theoretical yield based upon the metal salt. The size, size distribution, and shape of the resulting nanocrystals were determined by TEM. The core composition of the nanocrystals were determined through a combination of XRD and XPS. The composition of the ligand shells were determined by ToF-SIMS and XPS. The results of these measurements are provided in the Results and Discussion,

and spectra are found in the Supporting Information. The average compositions based upon these data are provided at the end of each preparation below.

**Synthesis of Oleic Acid-Stabilized Indium Oxide Nanocrystals (1).** Nanocrystals were prepared using the standard preparation outlined above. Briefly, indium(III) acetate (0.292 g, 1 mmol) was mixed with oleic acid (2 mL), then heated at 150 °C for 1 h under flowing nitrogen to produce a clear, yellowish solution of indium oleate. This solution was added to oleyl alcohol (12.5 mL) at 0.2 mL/min. During addition of the indium oleate precursor, the color of the reaction mixture changed from clear to bluish and then to light yellow that persists throughout the 20 min heating period. After cooling to room temperature, precipitation, and washing, the nanocrystals were collected by dissolving the residue in toluene and then evaporating the solvent by rotoevaporation to yield 159 mg (97% yield calculated for the indium oxide core) of light yellow solid. The resulting nanocrystals are 7.2 nm (±0.7 nm) $In_2O_3$(oleic acid)$_{98\%}$(oleyl alcohol)$_{2\%}$.

**Synthesis of Oleic Acid-Stabilized Iron Oxide Nanocrystals (2).** Nanocrystals were prepared using the standard preparation outlined above. Briefly, iron(II) acetate (0.174 g, 1 mmol) was mixed with oleic acid (2 mL), then heated at 150 °C for 30 min under flowing nitrogen to produce a clear brown solution of iron oleate. This solution was added to oleyl alcohol (12.5 mL) at 0.2 mL/min. During addition of the iron oleate precursor, the color of the reaction mixture changed from a clear to a dark brown dispersion of iron oxide nanocrystals that persists throughout the 20 min heating period. After cooling to room temperature, precipitation, and washing, the nanocrystals were collected by dissolving the residue in toluene and then evaporating the solvent by rotoevaporation to yield 90 mg (80% yield, calculated for iron oxide core) of a dark brown solid. The resulting nanocrystals are 4.0 nm (±0.3 nm) $\gamma$-$Fe_2O_3$(oleic acid)$_{89\%}$(oleyl alcohol)$_{11\%}$.

**Synthesis of Oleic Acid-Stabilized Manganese Oxide Nanocrystals (3).** Nanocrystals were prepared using the standard preparation outlined above. Briefly, manganese(II) acetate (0.173 g, 1 mmol) was mixed with oleic acid (2 mL), then heated at 150 °C for 30 min under flow of nitrogen to produce a clear brownish solution of manganese oleate. This solution was added to oleyl alcohol (12.5 mL) at 0.2 mL/min. During addition of the manganese oleate precursor, the color of the reaction mixture changed from a clear to a dark brown dispersion of manganese oxide nanocrystals. After cooling to room temperature, precipitation, and washing, the nanocrystals were collected by dissolving the residue in toluene and then evaporating the solvent by rotoevaporation to yield 76 mg (81% yield calculated for $Mn_3O_4$) of a dark brown solid. The resulting nanocrystals are 9.2 nm (±1.1 nm) $Mn_3O_4$(oleic acid)$_{93\%}$(oleyl alcohol)$_{7\%}$.

**Synthesis of Oleic Acid-Stabilized Cobalt Oxide Nanocrystals (4).** Nanocrystals were prepared using the standard preparation outlined above. Briefly, cobalt(II) acetate (0.177 g, 1 mmol) was mixed with oleic acid (2 mL), then heated at 150 °C for 30 min under flow of nitrogen to produce a clear violet solution of cobalt oleate. This solution was added to oleyl alcohol (12.5 mL) at 0.2 mL/min. During addition of the cobalt oleate precursor, the color of the reaction mixture changed from a clear to a dark brown and then a blackish dispersion of cobalt oxide nanocrystals that persists throughout the 20 min heating period. After cooling to room temperature, precipitation, and washing, the nanocrystals were collected by dissolving the residue in toluene and then evaporating the solvent by rotoevaporation to yield 80 mg (72% calculated for cobalt oxide core) of a black solid. These nanocrystals slowly precipitate out of toluene dispersions with time. The resulting nanocrystals are 6.6 nm (±1.6 nm) CoO(oleic acid)$_{93\%}$(oleyl alcohol)$_{7\%}$.

**Synthesis of Oleic Acid-Stabilized Zinc Oxide Nanocrystals (5).** Nanocrystals were prepared using the standard preparation outlined above. Briefly, zinc(II) acetate (0.183 g, 1 mmol) was mixed with oleic acid (2 mL), then heated at 150 °C for 30 min under a flow of nitrogen to produce a light yellowish solution of zinc oleate. This solution was added to oleyl alcohol (12.5 mL). Since zinc oleate precipitates below 70 °C, the solution was kept at 150 °C during the addition which was performed using a warm Pasteur pipet at about 0.2 mL/min. The color of the reaction mixture changed from a clear to a light yellowish dispersion of zinc oxide nanocrystals. After cooling to room temperature, precipitation, and washing, the nanocrystals were collected by dissolving the residue in toluene and then evaporating the solvent by rotoevaporation to yield 45 mg (33% yield based upon the ZnO core) of a yellowish solid. The nanocrystals precipitate out of toluene dispersions over time. The resulting nanocrystals are 5.6 nm (±1.0 nm) ZnO(oleic acid)$_{92\%}$(oleyl alcohol)$_{8\%}$.

**Synthesis of Oleic Acid-Stabilized 10% Tin-Doped Indium Oxide Nanocrystals (6).** Nanocrystals were prepared using the standard preparation outlined above for indium acetate, substituting tin acetate for a portion of the indium acetate. Briefly, indium(III) acetate (0.9 mmol) and tin(IV) acetate (0.1 mmol) were mixed with oleic acid (2 mL), then heated to 150 °C for 30 min under a flow of nitrogen to produce a yellowish clear solution of indium−tin oleate This solution was added to oleyl alcohol (12.5 mL) at 0.2 mL/min. During addition of the indium−tin oleate precursor, the color of the reaction mixture changed from a clear solvent to a yellowish then a dark blue dispersion of tin-doped indium oxide nanocrystals that persists throughout the 20 min heating period. The resulting nanocrystals are 6.3 nm (±0.6 nm) ($In_{89.5\%}Sn_{10.5\%}$)(oleic acid)$_{98\%}$(oleyl alcohol)$_{2\%}$.

**Synthesis of Oleic Acid-Stabilized Iron Oxide/Manganese Oxide Core/Shell Nanocrystals (7).** For core/shell structures, the growth of the shell onto the preformed core is carried out using a similar procedure as for the main nanocrystal synthesis. Because oleyl alcohol is so viscous, to speed the dispersion of the nanocrystal powder (the isolated material from the preparation of **2**), a toluene dispersion of the nanocrystals was added into oleyl alcohol (12.5 mL) and the toluene was removed by rotary evaporation. The manganese oleate precursor, described in the preparation of **3**, was kept at 60 °C and hot-injected at 0.2 mL/min into oleyl alcohol (12.5 mL) that was already heated to 160 °C in a 50 mL three-necked flask under flowing nitrogen. The color of the reaction mixture remained a black clear dispersion throughout the addition and 20 min heating period.

**Synthesis of Zinc Oxide/Gallium Oxide Core/Shell Nanocrystals (9).** A toluene solution of the zinc oxide nanocrystals (the isolated material from the preparation of **5**), was added into oleyl alcohol (12.5 mL), and the toluene removed by rotary evaporation. Gallium(III) acetylacetate (1 mmol) was mixed with oleic acid (2 mL), then heated to 150 °C for 30 min under flowing nitrogen to produce a light yellowish dispersion of gallium oleate. The gallium oleate precursor was kept at 60 °C and hot-injected at 0.2 mL/min into oleyl alcohol that was already heated to 160 °C in a 50 mL three-necked flask with flowing nitrogen. During the addition of the gallium oleate precursor, the color of the reaction mixture changed from a light yellowish to a light blue solution that persists throughout the 20 min heating period.

*Conflict of Interest:* The authors declare no competing financial interest.

*Acknowledgment.* We thank S. Golledge for assistance in acquiring all XPS analysis and ToF SIMS data reported in this work and E. Richman for helpful discussions. We also thank S. Young for XRD analysis, A. Jansons for TGA analysis, Z. Kennedy for SAXS analysis, and J. Razink for EDX analysis. We gratefully acknowledge Sony Corporation (Japan) for their support of this research. Portions of this work were also supported by the Air Force Research Laboratory (under Agreement No. FA8650-05-1-5041). The CAMCOR TEM facility is supported in grants from the W.M. Keck Foundation, the M.J. Murdock Charitable Trust, the Oregon Nanoscience and Microtechnologies Institute, and the University of Oregon.

*Supporting Information Available:* NMR data for the esterification reaction, images of solutions of doped $In_2O_3$, $\gamma$-$Fe_2O_3$, and ITO nanocrystals, an image of the reaction setup, and XPS, XRD, EDX, and ToF-SIMS data for the nanocrystals. This material is available free of charge *via* the Internet at http://pubs.acs.org.

## REFERENCES AND NOTES

1. Zou, Z.; Ye, J.; Sayama, K.; Arakawa, H. Direct Splitting of Water under Visible Light Irradiation with an Oxide Semiconductor Photocatalyst. *Nature* **2001**, *414*, 625–627.

2. Yamada, Y.; Tsung, C.-K.; Huang, W.; Huo, Z.; Habas, S. E.; Soejima, T.; Aliaga, C. E.; Somorjai, G. A.; Yang, P. Nanocrystal Bilayer for Tandem Catalysis. *Nat. Chem.* **2011**, *3*, 372–376.
3. Poizot, P.; Laruelle, S.; Grugeon, S.; Dupont, L.; Tarascon, J. M. Nano-sized Transition-Metal Oxides as Negative-Electrode Materials for Lithium-Ion Batteries. *Nature* **2000**, *407*, 496–499.
4. Sun, Y.-K.; Chen, Z.; Noh, H.-J.; Lee, D.-J.; Jung, H.-G.; Ren, Y.; Wang, S.; Yoon, C. S.; Myung, S.-T.; Amine, K. Nanostructured High-Energy Cathode Materials for Advanced Lithium Batteries. *Nat. Mater.* **2012**, *11*, 942–947.
5. Mor, G. K.; Varghese, O. K.; Paulose, M.; Shankar, K.; Grimes, C. A. A Review on Highly Ordered, Vertically Oriented $TiO_2$ Nanotube Arrays: Fabrication, Material Properties, and Solar Energy Applications. *Sol. Energy Mater. Sol. Cells* **2006**, *90*, 2011–2075.
6. Wang, Z. L. ZnO Nanowire and Nanobelt Platform for Nanotechnology. *Mater. Sci. Eng., R* **2009**, *64*, 33–71.
7. Comini, E.; Faglia, G.; Sberveglieri, G.; Pan, Z.; Wang, Z. L. Stable and Highly Sensitive Gas Sensors Based on Semiconducting Oxide Nanobelts. *Appl. Phys. Lett.* **2002**, *81*, 1869–1871.
8. O'Dwyer, C.; Szachowicz, M.; Visimberga, G.; Lavayen, V.; Newcomb, S. B.; Sotomayor Torres, C. M. Bottom-up Growth of Fully Transparent Contact Layers of Indium Tin Oxide Nanowires for Light-Emitting Devices. *Nat. Nanotechnol.* **2009**, *4*, 239–244.
9. Ozgur, U.; Alivov, Y. I.; Liu, C.; Teke, A.; Reshchikov, M. A.; Dogan, S.; Avrutin, V.; Cho, S. J.; Morkoc, H. A Comprehensive Review of ZnO Materials and Devices. *J. Appl. Phys.* **2005**, *98*, 041301–041301−041103.
10. Bussian, D. A.; Crooker, S. A.; Yin, M.; Brynda, M.; Efros, A. L.; Klimov, V. I. Tunable Magnetic Exchange Interactions in Manganese-Doped Inverted Core-Shell ZnSe−CdSSe Nanocrystals. *Nat. Mater.* **2009**, *8*, 35–40.
11. Wang, F.; Deng, R.; Wang, J.; Wang, Q.; Han, Y.; Zhu, H.; Chen, X.; Liu, X. Tuning Upconversion through Energy Migration in Core−Shell Nanoparticles. *Nat. Mater.* **2011**, *10*, 968–973.
12. Matijevic, E. Monodispersed Metal (Hydrous) Oxides—A Fascinating Field of Colloid Science. *Acc. Chem. Res.* **1981**, *14*, 22–29.
13. Matijevic, E. Preparation and Properties of Uniform Size Colloids. *Chem. Mater.* **1993**, *5*, 412–426.
14. Niederberger, M.; Garnweitner, G.; Pinna, N.; Neri, G. Nonaqueous Routes to Crystalline Metal Oxide Nanoparticles: Formation Mechanisms and Applications. *Prog. Solid State Chem.* **2005**, *33*, 59–70.
15. Niederberger, M. Nonaqueous Sol−Gel Routes to Metal Oxide Nanoparticles. *Acc. Chem. Res.* **2007**, *40*, 793–800.
16. Debecker, D. P.; Mutin, P. H. Non-hydrolytic Sol−Gel Routes to Heterogeneous Catalysts. *Chem. Soc. Rev.* **2012**, *41*, 3624–3650.
17. Garnweitner, G.; Niederberger, M. Organic Chemistry in Inorganic Nanomaterials Synthesis. *J. Mater. Chem.* **2008**, *18*, 1171–1182.
18. Adireddy, S.; Lin, C.; Palshin, V.; Dong, Y.; Cole, R.; Caruntu, G. Size-Controlled Synthesis of Quasi-Monodisperse Transition-Metal Ferrite Nanocrystals in Fatty Alcohol Solutions. *J. Phys. Chem. C* **2009**, *113*, 20800–20811.
19. Garnweitner, G.; Niederberger, M. Nonaqueous and Surfactant-Free Synthesis Routes to Metal Oxide Nanoparticles. *J. Am. Ceram. Soc.* **2006**, *89*, 1801–1808.
20. Sun, S.; Zeng, H.; Robinson, D. B.; Raoux, S.; Rice, P. M.; Wang, S. X.; Li, G. Monodisperse $MFe_2O_4$ (M = Fe, Co, Mn) Nanoparticles. *J. Am. Chem. Soc.* **2003**, *126*, 273–279.
21. Jana, N. R.; Chen, Y.; Peng, X. Size- and Shape-Controlled Magnetic (Cr, Mn, Fe, Co, Ni) Oxide Nanocrystals *via* a Simple and General Approach. *Chem. Mater.* **2004**, *16*, 3931–3935.
22. Park, J.; Joo, J.; Kwon, S. G.; Jang, Y.; Hyeon, T. Synthesis of Monodisperse Spherical Nanocrystals. *Angew. Chem., Int. Ed.* **2007**, *46*, 4630–4660.
23. Lee, J.; Zhang, S.; Sun, S. High-Temperature Solution-Phase Syntheses of Metal-Oxide Nanocrystals. *Chem. Mater.* **2013**, *25*, 1293–1304.
24. Ito, D.; Masuko, K.; Weintraub, B.; McKenzie, L.; Hutchison, J. Convenient Preparation of ITO Nanoparticles Inks for Transparent Conductive Thin Films. *J. Nanopart. Res.* **2012**, *14*, 1–7.
25. Kwon, S. G.; Hyeon, T. Formation Mechanisms of Uniform Nanocrystals *via* Hot-Injection and Heat-up Methods. *Small* **2011**, *7*, 2685–2702.
26. Buonsanti, R.; Milliron, D. J. Chemistry of Doped Colloidal Nanocrystals. *Chem. Mater.* **2013**, *25*, 1305–1317.
27. Narayanaswamy, A.; Xu, H.; Pradhan, N.; Kim, M.; Peng, X. Formation of Nearly Monodisperse $In_2O_3$ Nanodots and Oriented-Attached Nanoflowers: Hydrolysis and Alcoholysis *vs* Pyrolysis. *J. Am. Chem. Soc.* **2006**, *128*, 10310–10319.
28. Gilstrap, R. A.; Capozzi, C. J.; Carson, C. G.; Gerhardt, R. A.; Summers, C. J. Synthesis of a Nonagglomerated Indium Tin Oxide Nanoparticle Dispersion. *Adv. Mater.* **2008**, *20*, 4163–4166.
29. Aracil, J.; Vicente, M.; Martinez, M.; Poulina, M. Biocatalytic Processes for the Production of Fatty Acid Esters. *J. Biotechnol.* **2006**, *124*, 213–223.
30. Yadav, G. D.; Mehta, P. H. Heterogeneous Catalysis in Esterification Reactions: Preparation of Phenethyl Acetate and Cyclohexyl Acetate by Using a Variety of Solid Acidic Catalysts. *Ind. Eng. Chem. Res.* **1994**, *33*, 2198–2208.
31. Singhal, A.; Achary, S. N.; Manjanna, J.; Chatterjee, S.; Ayyub, P.; Tyagi, A. K. Chemical Synthesis and Structural and Magnetic Properties of Dispersible Cobalt- and Nickel-Doped ZnO Nanocrystals. *J. Phys. Chem. C* **2010**, *114*, 3422–3430.
32. Kwon, S. G.; Hyeon, T. Colloidal Chemical Synthesis and Formation Kinetics of Uniformly Sized Nanocrystals of Metals, Oxides, and Chalcogenides. *Acc. Chem. Res.* **2008**, *41*, 1696–1709.
33. Caruntu, D.; Yao, K.; Zhang, Z.; Austin, T.; Zhou, W.; O'Connor, C. J. One-Step Synthesis of Nearly Monodisperse, Variable-Shaped $In_2O_3$ Nanocrystals in Long Chain Alcohol Solutions. *J. Phys. Chem. C* **2010**, *114*, 4875–4886.
34. Habulin, M.; Krmelj, V.; Knez, Ž. Synthesis of Oleic Acid Esters Catalyzed by Immobilized Lipase. *J. Agric. Food Chem.* **1996**, *44*, 338–342.
35. Ye, E.; Zhang, S.-Y.; Hon Lim, S.; Liu, S.; Han, M.-Y. Morphological Tuning, Self-Assembly and Optical Properties of Indium Oxide Nanocrystals. *Phys. Chem. Chem. Phys.* **2010**, *12*, 11923–11929.
36. Peng, X.; Manna, L.; Yang, W.; Wickham, J.; Scher, E.; Kadavanich, A.; Alivisatos, A. P. Shape Control of CdSe Nanocrystals. *Nature* **2000**, *404*, 59–61.
37. Park, S.; Lee, K.-S.; Bozoklu, G.; Cai, W.; Nguyen, S. T.; Ruoff, R. S. Graphene Oxide Papers Modified by Divalent Ions—Enhancing Mechanical Properties *via* Chemical Cross-Linking. *ACS Nano* **2008**, *2*, 572–578.
38. Taheri, P.; Wielant, J.; Hauffman, T.; Flores, J. R.; Hannour, F.; de Wit, J. H. W.; Mol, J. M. C.; Terryn, H. A Comparison of the Interfacial Bonding Properties of Carboxylic Acid Functional Groups on Zinc and Iron Substrates. *Electrochim. Acta* **2011**, *56*, 1904–1911.
39. Wang, L.; Luo, J.; Maye, M. M.; Fan, Q.; Rendeng, Q.; Engelhard, M. H.; Wang, C.; Lin, Y.; Zhong, C.-J. Iron Oxide-Gold Core-Shell Nanoparticles and Thin Film Assembly. *J. Mater. Chem.* **2005**, *15*, 1821–1832.
40. He, J.; Kanjanaboos, P.; Frazer, N. L.; Weis, A.; Lin, X.-M.; Jaeger, H. M. Fabrication and Mechanical Properties of Large-Scale Freestanding Nanoparticle Membranes. *Small* **2010**, *6*, 1449–1456.
41. Agoston, P.; Albe, K. Thermodynamic Stability, Stoichiometry, and Electronic Structure of BCC-$In_2O_3$ Surfaces. *Phys. Rev. B* **2011**, *84*, 045311.
42. Hu, W. B.; Tian, D. T.; Mi, Y. Z.; Nie, G. H.; Zhao, Y. M.; Liu, Z. L.; Yao, K. L. Synthesis and Characterization of $In_2O_3$ Nanocube *via* a Solvothermal-Calcination Route. *Mater. Chem. Phys.* **2009**, *118*, 277–280.
43. Tang, Q.; Zhou, W.; Zhang, W.; Ou, S.; Jiang, K.; Yu, W.; Qian, Y. Size-Controllable Growth of Single Crystal $In(OH)_3$ and $In_2O_3$ Nanocubes. *Cryst. Growth Des.* **2004**, *5*, 147–150.
44. Jeong, S.; Ha, Y.-G.; Moon, J.; Facchetti, A.; Marks, T. J. Role of Gallium Doping in Dramatically Lowering Amorphous-Oxide

Processing Temperatures for Solution-Derived Indium Zinc Oxide Thin-Film Transistors. *Adv. Mater.* **2010**, *22*, 1346–1350.
45. Li, L.; Yang, Y.; Ding, J.; Xue, J. Synthesis of Magnetite Nanooctahedra and Their Magnetic Field-Induced Two-/Three-Dimensional Superstructure. *Chem. Mater.* **2010**, *22*, 3183–3191.
46. Zhang, Y.; Zhu, J.; Song, X.; Zhong, X. Controlling the Synthesis of CoO Nanocrystals with Various Morphologies. *J. Phys. Chem. C* **2008**, *112*, 5322–5327.
47. Biesinger, M. C.; Payne, B. P.; Grosvenor, A. P.; Lau, L. W. M.; Gerson, A. R.; Smart, R. S. C. Resolving Surface Chemical States in XPS Analysis of First Row Transition Metals, Oxides and Hydroxides: Cr, Mn, Fe, Co and Ni. *Appl. Surf. Sci.* **2011**, *257*, 2717–2730.
48. Gilstrap, R. A., Jr; Summers, C. J. Synthesis and Analysis of an Indium Tin Oxide Nanoparticle Dispersion. *Thin Solid Films* **2009**, *518*, 1136–1139.
49. Ito, D.; Tomita, T.; Hatazawa, T. Room Temperature Observation of Negative Differential Resistance Effect Using ZnO Nanocrystal Structure with Double Schottky Barriers. *Appl. Phys. Lett.* **2007**, *90*, 143118–143113.
50. Rothschild, A.; Komem, Y. The Effect of Grain Size on the Sensitivity of Nanocrystalline Metal-Oxide Gas Sensors. *J. Appl. Phys.* **2004**, *95*, 6374–6380.
51. Ghosh Chaudhuri, R.; Paria, S. Core/Shell Nanoparticles: Classes, Properties, Synthesis Mechanisms, Characterization, and Applications. *Chem. Rev.* **2011**, *112*, 2373–2433.
52. Lee, K. S.; Anisur, R. M.; Kim, K. W.; Kim, W. S.; Park, T.-J.; Kang, E. J.; Lee, I. S. Seed Size-Dependent Formation of $Fe_3O_4$/MnO Hybrid Nanocrystals: Selective, Magnetically Recyclable Catalyst Systems. *Chem. Mater.* **2012**, *24*, 682–687.
53. Jeong, U.; Teng, X.; Wang, Y.; Yang, H.; Xia, Y. Superparamagnetic Colloids: Controlled Synthesis and Niche Applications. *Adv. Mater.* **2007**, *19*, 33–60.
54. Masala, O.; Seshadri, R. Spinel Ferrite/MnO Core/Shell Nanoparticles: Chemical Synthesis of All-Oxide Exchange Biased Architectures. *J. Am. Chem. Soc.* **2005**, *127*, 9354–9355.
55. Dabbousi, B. O.; Rodriguez-Viejo, J.; Mikulec, F. V.; Heine, J. R.; Mattoussi, H.; Ober, R.; Jensen, K. F.; Bawendi, M. G. (CdSe)ZnS Core−Shell Quantum Dots: Synthesis and Characterization of a Size Series of Highly Luminescent Nanocrystallites. *J. Phys. Chem. B* **1997**, *101*, 9463–9475.
56. Medintz, I. L.; Uyeda, H. T.; Goldman, E. R.; Mattoussi, H. Quantum Dot Bioconjugates for Imaging, Labelling and Sensing. *Nat. Mater.* **2005**, *4*, 435–446.
57. Xia, T.; Kovochich, M.; Liong, M.; Mädler, L.; Gilbert, B.; Shi, H.; Yeh, J. I.; Zink, J. I.; Nel, A. E. Comparison of the Mechanism of Toxicity of Zinc Oxide and Cerium Oxide Nanoparticles Based on Dissolution and Oxidative Stress Properties. *ACS Nano* **2008**, *2*, 2121–2134.
58. Hsiao, I. L.; Huang, Y.-J. Titanium Oxide Shell Coatings Decrease the Cytotoxicity of ZnO Nanoparticles. *Chem. Res. Toxicol.* **2011**, *24*, 303–313.
59. Ito, D.; Jespersen, M. L.; Hutchison, J. E. Selective Growth of Vertical ZnO Nanowire Arrays Using Chemically Anchored Gold Nanoparticles. *ACS Nano* **2008**, *2*, 2001–2006.
60. Xiang, B.; Wang, P.; Zhang, X.; Dayeh, S. A.; Aplin, D. P. R.; Soci, C.; Yu, D.; Wang, D. Rational Synthesis of P-Type Zinc Oxide Nanowire Arrays Using Simple Chemical Vapor Deposition. *Nano Lett.* **2006**, *7*, 323–328.
61. Binet, L.; Gourier, D. Origin of the Blue Luminescence of $\beta$-$Ga_2O_3$. *J. Phys. Chem. Solids* **1998**, *59*, 1241–1249.
62. Chang, K.-W.; Wu, J.-J. Formation of Well-Aligned $ZnGa_2O_4$ Nanowires from $Ga_2O_3$/ZnO Core−Shell Nanowires *via* a $Ga_2O_3$/$ZnGa_2O_4$ Epitaxial Relationship. *J. Phys. Chem. B* **2005**, *109*, 13572–13577.
63. Sawada, Y.; Shigaraki, T.; Seki, S.; Ogawa, M.; Senda, T.; Nishide, T.; Matsushita, J.-i. TG-DTA-MS of Indium Acetate. *J. Mass Spectrom. Soc. Jpn.* **1998**, *46*, 292–295.